Benjamin Meiner,
Calder Leppitsch,
Levi Sheridan,
Ariel Tamayev
Mechanical Engineering,
The Cooper Union for the Advancement of Science and Art,
41 Cooper Square,
New York, NY, USA

Dr. Dirk Martin Luchtenberg,
Dr. David Wootton
Advisors,
Professors of Mechanical Engineering

Cooper Union Vertical Flight

The Cooper Union Vertical Flight (CUVF) team's objective is to design and manufacture an aerial vehicle capable of competing in the Vertical Flight Society (VFS) Design-Build-Vertical-Flight (DBVF) competition. Our design improves the classic quadcopter setup by adding an angled wing to maintain a perfect horizontal position during forward flight. This takes advantage of the lift of vertical propellers and the efficiency of the wing in horizontal flight and allows for a seamless transition between flight modes. The slight tilt of the wing compensates for the aircraft's forward tilt induced by the vertical propulsion system, enabling both the quadcopter's propellers and the wing to generate lift during forward flight. This approach not only simplifies control mechanisms but also adheres to stringent competition regulations regarding weight and size, ensuring the aircraft's competitive edge and compliance.

1 Introduction

1.1 Background. Vertical take-off and landing (VTOL) aircraft came into conception with the development of the helicopter during the Second World War. In the decades following, the field grew rapidly as aerospace contractors researched the many possible configurations. Several renowned solutions that fall in this class of vehicle are the Bell Boeing V-22 Osprey (Figure 1), the Hawker Siddeley Harrier Jet, and Lockheed Martin F-35 Lightning II [1]. These aircraft demonstrate the diversity of approaches used in accomplishing mission goals where VTOL is required. Many such vehicles are sold to and used exclusively by military entities.

Fig. 1 Bell Boeing V-22 Osprey

On the other hand, there has historically been less demand for VTOL innovations in other applications. The commercial aviation transportation industry is serviced excellently by large jets which take off and land on long runways. Conventional helicopters are often used for search and rescue missions as well as personal transport. Unmanned quadcopter drones carved a niche in surveillance, infrastructure inspection, and ecological assessment due to their loitering capability. Interest in larger format VTOL aircraft for civilian applications was not present. This changed with the advent of electric cars, as many companies identified a business opportunity in developing electrically powered VTOL (eVTOL) aircraft as a sustainable option for solving transportation needs. Recent advancements in battery technologies and more efficient propulsion systems allow eVTOL to be an affordable way to address demand for rapid urban transportation and delivery services, search and rescue, and military uses. The past decade has seen companies including Archer, Joby, Lilium, and Vertical developing a variety of designs for this class of vehicles [2].

The Vertical Flight Society (VFS) is a non-profit society working towards the advancement of vertical flight. They host events such as forums and competitions to grow technology and industry. The mission for this capstone project is to participate in the Design-Build-Vertical Flight Competition (DBVF) which challenges student teams from universities across the world to design and build their own unmanned eVTOL.

Fig. 2 Vertical Flight Society Logo

1.2 Motivation. The team wanted to take on this challenge because designing and building an aircraft from scratch requires a culmination of all the knowledge gained through the mechanical engineering curriculum. It also allows each of the team members room to grow deeper knowledge in specialty areas such as aerodynamics, controls, and electronics independent from the lecture environment. The framework of the competition incentivizes solutions that are efficient in terms of weight and aerodynamic performance. This is measured by a greater payload to aircraft weight ratio and a faster lap speed. The problem of developing an efficient aircraft is quite open-ended, as indicated by the large variety of solutions in the VTOL space [3]. To tackle the problem, this capstone project favors a simplistic approach which serves the

Version 1.18, May 7, 2024

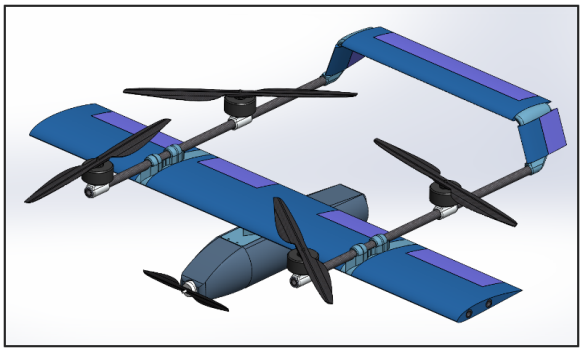

Fig. 3 Initial Design Concept

goal of accomplishing the entire design, construction, and testing sequence within the space of two semesters. Although simplification of the problem could result in overlooking design flaws, the low-risk environment allows us to learn equally through failure and iteration.

1.3 Design Concept. The DBVF competition consists of both vertical flight and forward flight portions. Combining the two flight modes into a single vehicle is the challenge that prompts so many options for the design space. The design chosen in this project uses four propellers in a quadcopter configuration with a single wing spanning the vehicle laterally. This concept in theory allows for a simple transition during which the vehicle pitches forward just like a typical quadcopter. As the speed of the aircraft increases, so does the lift generated by the wing, reducing the thrust and power consumption required of the propellers. The transition back from forward flight to vertical flight occurs in a similar manner. The vehicle pitches backward and as the aircraft's horizontal velocity decreases, the vertical flight propellers provide the excess thrust to keep the aircraft in the air.

There were several critical considerations and choices involved when deciding on aircraft shape, placement of propellers, and overall goal. The initial design concept is featured in Figure 3. The choice to go with a rectangular wing was made since it would allow for simplicity in design, analysis, and manufacturing. One of the main goals of the design and manufacturing process was to make the aircraft modular using easily replaceable 3D printed sections. A complicated wing geometry does not allow this to be implemented. The next choice in this design was to have 4 vertical lift propellers. This choice was made for optimal stability and control. Any fewer propellers eliminates independent control of rotational degrees of freedom and any more propellers contribute unnecessary weight. The initial design concept created by the team had a dedicated forward flight propeller to avoid the complexities of designing a mechanism that tilts the vertical flight propellers. The tail provided the necessary moment to balance the wing like in a standard fixed wing aircraft. Typical aircraft control surfaces can be employed for control. The benefit of this design is that the vertical lift propellers can be shut off while the aircraft relies on the front propeller and the wing to produce the required lift. Turning the vertical propellers off completely saves a lot of battery energy and increases the overall efficiency leading to better performance in the competition.

In the current design the forward flight propeller and the tail are removed along with the control surfaces, leaving the vertical lift propellers responsible for horizontal flight and control. Several factors led to this decision. Removing the tail, horizontal propeller, and control surfaces reduces the amount of prototyping needed for those critical components allows more time for testing. In addition, controlling the aircraft in a quadcopter configuration is more stable as the risk of stalling is reduced when the propellers stay on the entire flight. If stall occurs during testing and the vehicle crashes, it compromises expensive equipment and manufacturing time.

1.4 Technical Innovations. In the research done for this project, this design utilizing a fixed wing as well as a quadcopter configuration was not found in the prior art. If successful, it could prove to be a clever adaptation to the classic quadcopter design that increases overall efficiency for longer distance missions. However, its performance must be evaluated through testing.

2 Design Constraints

The team is competing in the 2023-24 VFS DBVF which includes several deliverables. This includes a Submission Letter due in October 2023, a Final Technical Report due March 4, 2024, and an in-person Competition Fly-off at Harford Airport in Churchville, Maryland, from April 10-12, 2024. The fly-off is a culmination of the design and construction work where student teams bring their physical aircraft to be assessed by the judges.

The fly-off is preempted by safety checks of the operation of the vehicle to ensure it complies with all regulations specified in the DBVF documentation. This includes proper battery type of unaltered commercially available LiPo batteries of six cells (6S) or less, with the option of placing multiple batteries in parallel for the propulsion system. The remote control must demonstrate lost-link power-cut functionality. A failsafe system that cuts throttle to zero on signal loss is one way to meet this requirement. There must also be a remote-kill functionality during autonomous flight mode. The propulsion system and flight controller must have separate batteries. The aircraft must be equipped with a red shunt plug, whose purpose is to provide an easy and quick way to manually disarm the aircraft. The shunt plug must be wired between the leads of the battery system and the electronic speed controller for manual disarming and arming of the aircraft's power system. The shunt plug must be removable with only one hand and without any tool. The aircraft must weigh under 20 pounds and fit within a 10-foot diameter sphere. The judge performing the safety check will also evaluate the structural integrity and rigidity of the aircraft.

Once the safety checks are completed, the fly-off begins with a flight performance course. For the flight performance course, the vehicle is loaded with a minimum of 2 pounds of SoftGrip weights attached by a safety wire. A greater amount of payload weight carried by the aircraft results in a higher score, although the take-off weight must remain below 20 pounds. The aircraft begins at the center of a 30-foot diameter landing zone (LZ). One lap of the course consists of a vertical takeoff from the LZ, horizontal flight for 300 meters, a 180° turn, 350 meters of horizontal flight, another 180° turn, and a final 50 meters of horizontal flight before returning to the LZ and landing vertically. At the beginning/end of each lap, the vehicle must contact the ground and stop moving, although the rotors may still be spinning. The time limit for the course is 10 minutes, and a portion of the score is determined by the number of laps completed.

The second portion of the fly-off is an autonomous test. For the autonomous test, GPS coordinates representing the trajectory flown in the performance course are provided to the teams. These waypoints must be entered into the teams' ground control software and used to autonomously command the vehicle's flight path. The vehicle must complete just one lap of the course in autonomous mode. At the end of the fly-off is a 10-minute final presentation during which teams explain their design and production process [4].

2.1 Relevant Codes and Regulations. In order to participate in the competition, the team pilot must hold an FAA Part 107 license. This license ensures that proper safety is taken and all rules and regulations related to flying an unmanned aircraft are taken. Topics such as weather reports, reading sectional charts, what steps to take before flying the aircraft, and what to do in problematic circumstances are included on the exam. Both Calder Leppitsch and Benjamin Meiner passed this exam to become licensed pilots. They ensure during testing and competition all actions of the team are carried out in a manner which aligns with the FAA Regulations.

The NFPA 70-E standard on Electrical Safety in the Workplace is another relevant code that is important for the project. When dealing with high voltage or amperage, safety is of utmost importance. During the competition we discovered part of the circuitry was shorting and wires were getting very warm. This is very dangerous and can cause damage to components or even worse, harm the team. Taking proper precautions with electronics is necessary and the use of a shunt plug is one way to ensure all power is cut before touching anything on the plane.

FAA Regulations require that the aircraft be registered with the FAA and be marked with its registration number. The Federal Communications Commission Part 15 rules for transmission frequencies and International Telecommunication Union specify that telemetry, video, and control transmitters must operate on 901-928 MHz, 2.4 GHz, or 5.8 GHz [5].

FAA Regulations provide strict restrictions on airspace. This provides a significant obstacle for the team when it comes to testing. The number of Class G airspaces in New York City is very limited and requires membership and coordination with existing model airplane groups. To reach a location where flying a registered UAV without prior authorization is legal, it is necessary to drive upstate, out on Long Island, or into New Jersey. In those areas there exist parks and fields in Class G airspace which are far enough from people to be a safe testing environment.

3 Analysis

3.1 Wing Lift and Drag Analysis. Several airfoils are analyzed and simulated to determine which is be best for the design of the aircraft. At first, the computer program Xflr5 is used to find lift and drag coefficients for various airfoils. These airfoils are chosen since they are typical in model aircraft wings and cover a wide variety of airfoil types. These include the NACA 2412, NACA 2415, NACA 4415, Clark Y, and S1223 airfoils. Figure 4 compares the lift coefficient of the simulated airfoils at the design speed of $15 m/s$.

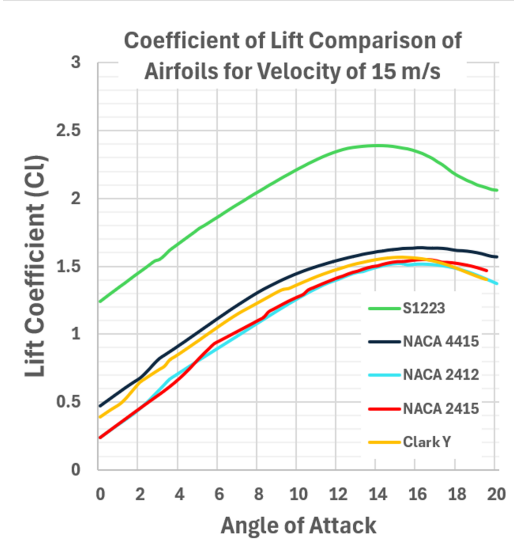

Fig. 4 Airfoil Lift Comparison

Since the S1223, NACA 4415 and Clark Y airfoils all produce the highest lift and highest lift to drag ratios, they are chosen to conduct further analysis. A full wing simulation is performed in Xflr5 to produce lift and drag coefficients that can be used to calculate what lift and drag forces will be expected. The resulting values are summarised in Table 1

The S1223 airfoil produces 62.8 N of force while the aircraft weighs 89 N. The other airfoils, while they produce much less drag, have considerably less lift. To yield an equivalent amount of lift, the wing would have to be almost double the wingspan. This is not feasible for structural considerations and would require adding significant weight to the aircraft. Therefore, an upper limit of 1.5 meters for the wingspan was set. The drag that the S1223 airfoil creates can easily be countered by the propellors and the increase in lift will greatly increase efficiency. It is for this reason that the S1223 is the final choice of airfoil.

	S1223	NACA 4415	Clark Y
C_L	1.52	0.92	0.86
Lift (N)	62.8	38.0	35.6
C_D	0.11	0.035	0.0032
Drag (N)	4.5	1.4	1.3

Table 1 Lift and Drag Summary

The angle of attack of 7 degrees is high and close to stall for normal aircraft. There are two main reasons why it shouldn't cause problems for this design. First, the aircraft takes off vertically and does not need to pitch itself upwards to lift off, risking stall. Second, the vertical propellers act as a failsafe if stall occurs during horizontal flight.

It is worth noting why a higher lift is not desired. If a slightly larger chord or angle of attack is chosen, more lift can be generated and perhaps fully equate to the weight of the aircraft. This is not desirable since if the wing lift perfectly balances the weight, the propeller's control authority will not be independent of the aircraft's altitude. Any increase in thrust to adjust for disturbances causes the vehicle to climb higher. Some leftover weight should be carried by the propellers and in this case about 26 N is the target.

3.2 Wing Structural Analysis. To ensure that the structure of the aircraft can withstand the various loads during flight a structural analysis is necessary. The wings are the main load bearing component of the aircraft. While the aircraft is stationary, they have to bear the weight of the motors at the wing tips. During flight, there are many more forces contributing to the total load. There are two scenarios to be considered: vertical takeoff and horizontal flight.

During horizontal flight there are several forces on the aircraft as shown in Figure 5. There is the weight of the aircraft pulling it downwards from the center of mass and opposing that is the lift force and the propeller force. The propeller force acts at the wing tips, while the lift force is distributed across the wingspan. For the analysis, all forces can be taken about the center of the fuselage. For vertical flight, the analysis is simpler, there is just a propeller force upwards, and the weight downwards, where the propeller force must be greater. If the maximum vertical acceleration is $2 m/s^2$, a total thrust force of around 107 N is required. This leads to a thrust of 53.5 for each side of the wing.

To obtain the vertical lift distribution, the program OpenVSP is used. The wing size and S1223 airfoil are put into the program and simulated using the vortex lattice method. The graph in Figure 6 is the data post-processed in Excel and fit to a fourth order polynomial trendline.

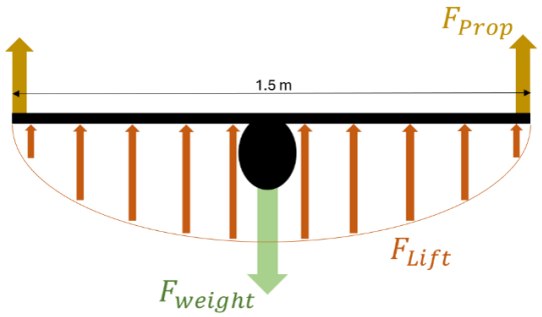

Fig. 5 Aircraft Forces

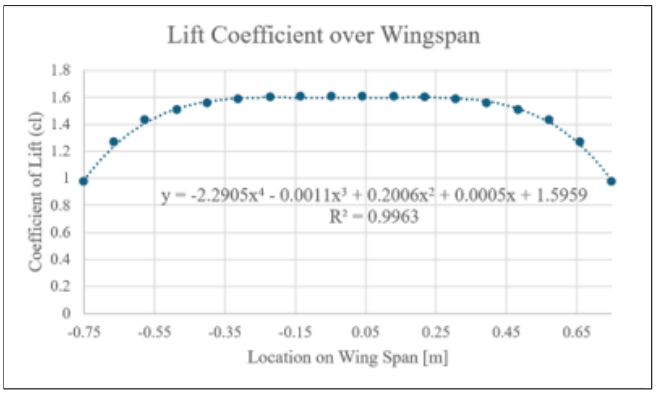

Fig. 6 Wing Lift Distribution

Using the lift coefficient, the force of lift distributed along the wing is calculated and integrated over the length to get the shear force in the beam. Note that since the wing is symmetrical, the centerline of the plane can be treated as a fixed point and each half of the wing can be treated as a cantilevered beam model. This shear only takes lift forces into account from the wing, however there is also lift force generated by the propellers. The propellers add whatever portion of the weight that hasn't been lifted from the wings. The average lift coefficient of 1.48 is used in Equation 1 to determine the total lift generated by the wing.

$$F_{\text{wings}} = 0.5 \times 1.48 \times 1.225 \frac{\text{kg}}{\text{m}^3} \times (15 \frac{\text{m}}{\text{s}})^2 \times 0.3\,\text{m}^2 \tag{1}$$

$$F_{\text{wings}} = 61.2N = 14lb$$

Therefore, an extra 3 pounds of lift must be provided by each set of propellers. This can simply be added to the shear force plot since for a cantilevered beam with a force on the end, the shear force is uniform and equal to the tip force.

The shear force is integrated to obtain the moment distribution, with the boundary condition that the moment is zero at the wing tip. Using classical beam theory and integrating several times, the deflection is obtained using Equations 2, 3 and 4.

$$\frac{dV}{dx} = -w \tag{2}$$

$$\frac{dM}{dx} = V \tag{3}$$

$$\frac{d^2y}{dx^2} = \frac{M(x)}{EI} \tag{4}$$

The contribution of stiffness from the lightweight PLA is neglected. The moment of inertia is simply the sum of the MOI for each circular carbon fiber beam. Young's Modulus, E, is estimated from the supplier's information. Figure 7 and Figure 8 summarize the findings from this analysis for both horizontal flight and vertical flight.

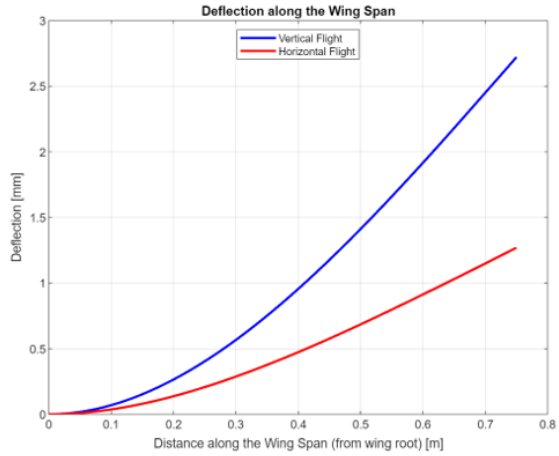

Fig. 7 Wing Deflection Distribution

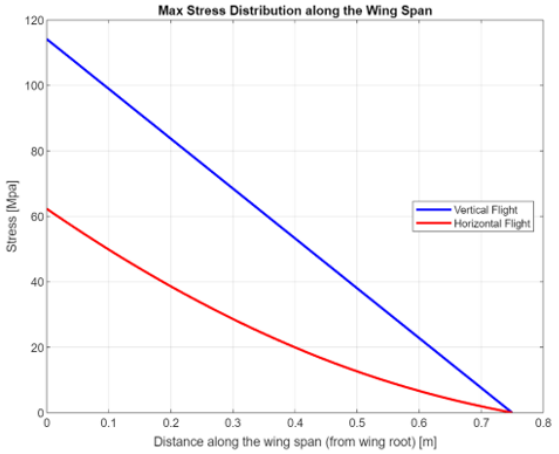

Fig. 8 Wing Stress Distribution

The maximum deflection for vertical flight is 2.6 mm, while the maximum deflection for horizontal flight is 1.27 mm. Both these values are small enough that wing deflection does not pose a concern during flight. The maximum normal stress is predicted as 115 MPa in vertical flight which is less than the manufacturer's specification tensile strength of about 860 MPa. This gives a factor of safety of 7.5 and even greater during the horizontal flight portion. Failure of the carbon fiber beams should not occur under these loading conditions and since the carbon fiber beams can take all the load, the 3D printed wing sections should not be under high stress as desired.

3.3 Motor and Propeller Analysis. The assumption is made that the vehicle on lift-off will weigh approximately 20lbf or 89N. This is a reasonable assumption because no matter the weight of the vehicle, the excess will be provided by the payload weight. This will in turn maximize the payload weight and increase the competition score. Working backwards from this assumption, it is simpler to specify the motor types that can produce sufficient thrust for both hovering and lift-off flight conditions.

The vertical flight propellers are in a quadcopter configuration, meaning that they must each provide a minimum 22.25N of thrust for hover. To understand the desired acceleration for vertical flight, it is relevant to consider the amount of time it takes for the drone to go from a standstill to final vertical speed. The chosen operational vertical speed of the vehicle is $2m/s$. A reasonable time for the acceleration procedure is 1 second, leading to an acceleration

value of $2m/s^2$. To obtain this acceleration in vertical flight, the motors must produce 26.78N of thrust each neglecting drag during the acceleration phase. The required thrust from each motor to maintain this velocity is 22.64N. This corresponds to a power draw of 395W and 320W.

Figure 9 shows a few motors that meet the thrust requirements. For this table, a single point close to the thrust required to maintain $2m/s$ in vertical flight is extracted from each thrust test curve. Out of these options, T-Motor and MAD Motors provide the most detailed documentation on thrust testing. Out of the T-Motor and MAD Motors options, the P60 and 5015 are the most efficient with power usage. The 5015 by MAD Motors is clearly superior, however, due to the lighter weight and smaller diameter. Another factor to consider is the previous year's team already purchased three of the P60 motors from T-Motor. This considerably reduces the overhead cost as each motor costs around $100. If this project was starting from a completely clean slate, the 5015 is a superior motor. One large downside of going with the easily accessible choice is they weigh the most out of all the options, reducing the final score due to limitations on the amount of payload that the aircraft can carry. Despite this, the team is moving forward with the T-Motor P60 KV340 motor and 20*6 Carbon Fiber propellers as vertical flight propulsion (Figures 10 and 11).

Motor Name	Motor Manufacturer	Propellor Name	Prop Manufacturer	Voltage	Throttle	Current	Power	Thrust (gf)
P60 KV340	T-Motor	20*6CF	T-Motor	24	60	14.5	348	2472
MN4116 KV450	T-Motor	P15*5	T-Motor	24	70	16.08	380	2340
MN501S KV240	T-Motor	P15*5	T-Motor	48	66	9.11	442	2421
CM-4510/40 310Kv	Cobra	16x5.5-MR	APC	22.2	NA	12.8	284	2181
CM-4520/18 310Kv	Cobra	16x5.5-CF	RC-Timer	18.5	NA	23.9	442.2	2620
5015 IPE V3.0 320KV	MAD Motors	Fluxer Matt Pro 20x6	MAD Motors	24	70	14.34	340.3	2585

RPM	Thrust Efficiency gf/W	Motor Mass (g)	Motor Diameter (mm)	Motor Cost (USD)	Propellor Mass (g)	Propellor Diameter (mm)	Propellor Cost (USD)
4491	7.10	375	69	108	47	508	54.45
6648	6.16	212	47.4	100	21	381	27.95
6960	5.47	170	55.6	100	21	381	27.95
5354	7.68	211	54.9	75	43.9	406.4	8.3
5042	5.93	340	54.9	95	24	406.4	11
4438	7.60	226	56	108	47	508	50

Fig. 9 Motor Options

Fig. 10 T-Motor P60 KV340

Fig. 11 T-Motor 20*6 CF

3.4 Horizontal Flight. To obtain horizontal flight while increasing energy efficiency, the thrust provided by the motors is augmented by a wing that reaches our desired angle of attack when the vehicle is pitched forward by some angle theta. To determine this value, a steady state model of the horizontal flight mode is approximated. The force-body diagram in Figure 12 demonstrates the balance between each of the forces acting on the vehicle. In steady horizontal flight, there is zero net force acting on the vehicle and it continues moving horizontally at a constant velocity. In the vertical direction, the weight of the vehicle is opposed by the wing's lift and the component of thrust $T\cos(\theta)$. In the horizontal direction, the drag on the vehicle is opposed by the component of thrust $T\sin(\theta)$.

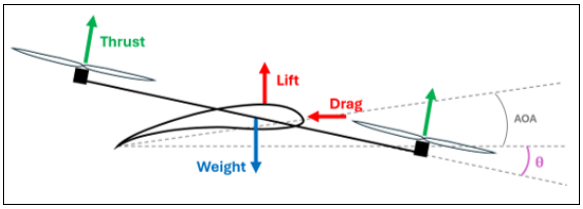

Fig. 12 Free Body Diagram of Vehicle

Solving this set of equations for the thrust-velocity pairs that satisfy the equilibrium over a set of angles theta produces the plot seen in Figure 13. The operating point of 12 degrees theta is chosen to provide a high degree of energy consumption efficiency relative to a pure hovering mode while not letting the lift component from the wing completely dominate the component produced by the motors. The horizontal velocity at the design point is $14.5m/s$ and the electrical consumption per motor is $103W$.

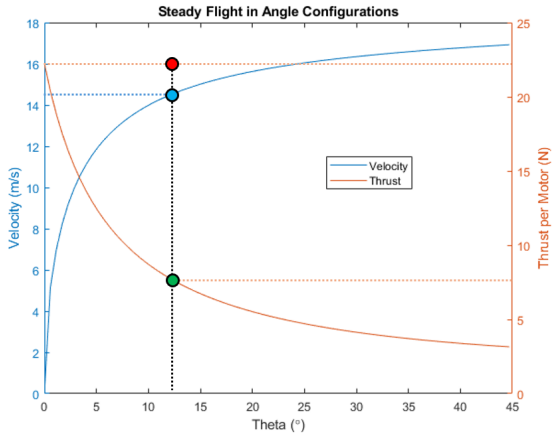

Fig. 13 Forward Flight Design Point

3.5 Battery Consumption. The battery energy capacity is calculated using the mission plan, flight speeds, and motor specifications. The longest duration mission is the flight performance course, which requires at least ten minutes of battery life. During each lap of this mission, there are several stages. The first is the vertical liftoff portion, which leads to a flight transition section from vertical to horizontal flight. For this analysis, it is assumed that the vehicle will rise to an altitude of 15 meters before flying horizontally. The vehicle then flies in 350-meter-long rectangular loop before returning to the landing zone to complete the lap.

In each phase of the flight, the motors will be using a varying amount of power as the plane accelerates and performs the required maneuvers. To calculate the total required energy provided by the battery over the flight mission, the amount of time spent operating in each phase can be multiplied by a constant power value determined by the stage's conditions. This power value is determined

by equating the thrust required of the motors to the current draw using the manufacturer's specifications. Summing the energy components from each stage results in the total energy usage for one lap of the course.

During the vertical portion of the flight, it is assumed that the vehicle flies to a height of 15 meters before transitioning to horizontal flight. This will occur over a time span of 8 seconds. The power usage during that time is $E_{V,L} = (4 \times 394.5W)(1s) + (4 \times 319.8W)(7s) = 10512Ws$. The horizontal portion of the flight is 350 meters which at a speed of $14.5m/s$ will be completed in 24 seconds. Assume the acceleration and deceleration phases of the horizontal flight path will increase the time of flight to 30 seconds. During this time, the power usage will be $E_{V,L} = (4 \times 103W)(30s) = 12360Ws$. The descent to the landing zone will be smoothly controlled by the vertical propulsion system providing thrust approximately equal to hover. The descent time will be approximately equal to the lift time of 8 seconds. The hovering thrust is 89N, corresponding to 313W/motor. The descent energy usage is $E_{V,D} = (4 \times 313W)(8s) = 10016Ws$. The total lap time is 46 seconds and allows us to complete 13 laps during the 10 minutes of competition. The total energy usage per lap is 32888Ws, resulting in a total power usage over the competition of 118Wh. At the voltage level of 24V required of the motors, a 6S LiPo battery is sufficient. The battery should at minimum therefore provide 5Ah of useful current. Figure 14 shows a variety of battery options that provide a factor of safety for our mission. The team chose to go with the HRB battery in Figure 27 as it had a high energy density and capacity for a decent price and weight.

Battery Manufacturer	Cells	Capacity (mAh)	Discharge Rate (C)	Dimensions (mm)	Weight (g)	Cost ($)	Connector	Energy Density
Turnigy	6S	10000	12	170x69x56	1320	102.4	XT90	7.57576
Turnigy	6S	12000	12	183x77x58	1650	122.88	XT90	7.27273
Turnigy	6S	12000	15	183x77x57	1610	125.95	XT90	7.45342
Glacier	6S	8000	30	170x164x145	1049	164.99	NA	7.62631
Gens Ace	6S	6800	100	165x47x68	955	159.99	EC5	7.12042
Tattu	6S	10000	30	176 x 66 x 58	1350	216.99	EC5	7.40741
Tattu	6S	12000	15	202 x 76 x 61	1670	282.99	EC5	7.18563
Tattu	6S	16000	15	230 x 81 x 70	2063	360.99	AS150+XT150	7.75570
HRB	6S	10000	25	165x64x63	1226	226	All	8.15661
HRB	6S	16000	25	180x70x63	1964	279.99	All	8.14664
SMC	6S	10800	120	71 x 50 x 160	1189	142.95	All	9.08326
Zeee	6S	7000	100	151x46x53.5	822	213.99	EC5	8.51582
Zeee	6S	10000	120	169x49x63	1150	305.99	EC5	8.69565

Fig. 14 Battery Options

4 Vehicle Design

The final airframe design is a mix between a traditional quadcopter and a flying wing, combining the advantages of both configurations. The vehicle employs four vertical flight propellers and a traditional quadcopter control scheme for locomotion, providing stability and maneuverability. A high-lift airfoil, integral to the structure of the aircraft, provides passive lift assistance while in forward flight, enhancing efficiency and endurance. The vehicle has a wingspan of 1.5 meters, offering ample lift and stability.

Located at the wing's center is a fuselage carrying the payload (Figure 15), battery, and autopilot hardware, ensuring optimal weight distribution and streamlined aerodynamics. At either wing tip is a 36-inch boom, on each end of the boom is one of the four vertical flight propellers. This layout is shown in Figure 16 and Figure 17. Adjacent to the wingtips are small compartments containing the two ESCs necessary to power the two motors on each wingtip boom. By relocating the ESCs to the wingtips, interference with the GPS sensor located in the fuselage is minimized, enhancing navigational accuracy. The wingtips are shown in Figure 18.

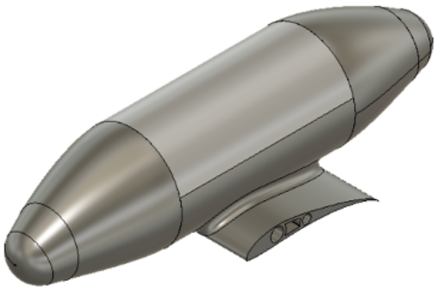

Fig. 15 Fuselage CAD

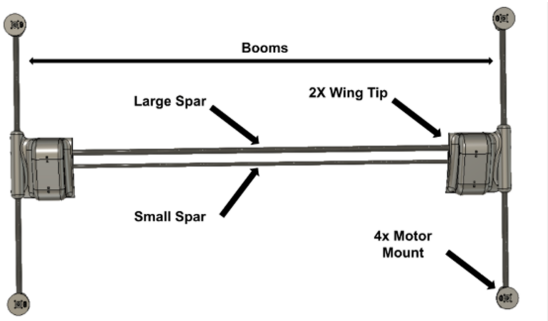

Fig. 16 Structural Arrangement

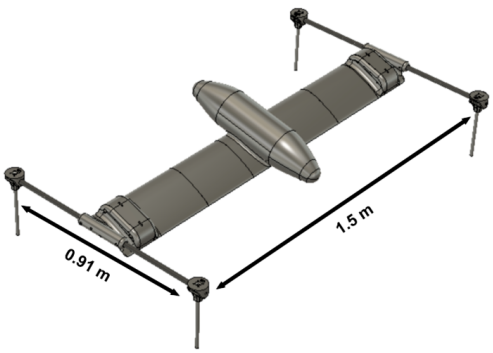

Fig. 17 Airframe Dimensions

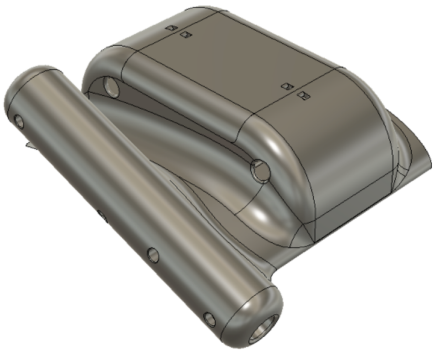

Fig. 18 Wingtip CAD

Overall, this airframe design combines innovative features from both quadcopter and flying wing configurations, resulting in a versatile and efficient aerial platform.

5 Fabrication

There were several manufacturing methods considered for the aircraft. Some typical aircraft fabrication methods at this scale are foam cutouts, carbon fiber layups, a wooden rib and sheet design or 3D printing. The manufacturing process of the vehicle that was desired was a method that significantly enhances design flexibility, rapid iteration, and ease of repair. Carbon fiber can be expensive and additionally does not allow for rapid iteration or ease of repairs. The foam cutout method is labor intensive, can limit design flexibility and is not a suitable choice for easy repairs. The rib and sheet design can be very strong and lightweight but has many more parts and is not conducive to rapid prototyping. It is for this reason that the 3D printing method is chosen as the main method for manufacturing. The two materials chosen for various parts of the vehicl are light-weight PLA and PETG.

5.1 Wing and Fuselage. The wing is constructed in individual sections, each designed for a specific function. These include boom mounts (wingtips), normal airfoil sections, and a fuselage section. The use of PLA and PETG allows for precise and customized manufacturing of each segment, catering to the specific aerodynamic and structural requirements of the vehicle. However, due to the lightweight printing technique desired, the 3D printed sections alone do not suffice and would break under loading. To assemble these sections into a cohesive and robust wing structure, carbon fiber spars are employed. These spars run the length of the wing, providing the necessary strength and rigidity while maintaining a low weight. This method of construction not only facilitates a modular design but also simplifies the process of making design modifications and repairs.

Light-weight PLA is chosen for the standard wing sections due to its reduced weight when compared to similar materials. An image of the wing cross-section is shown in Figure 19. This reduced weight allows the wing sections to be approximately 65 percent of the weight of a comparable PLA part. Furthermore, a single wall thickness design is implemented for the wing sections. Each wing section is printed in a spiral vase mode which enables the part to be made of a continuous, single wall-thickness path. This approach further minimizes the weight of the wing sections and decreases manufacturing time.

Fig. 19 Wing Section

A surface treating process is tested for the wing section in the hopes of creating a smoother and more well-finished aerodynamic surface as compared to the raw 3D print. The process includes first applying a layer of wood filler to the 3D print in order to fill in any major print lines. After the wood filler dries, it is lightly sanded before a primer filler is applied to the surface. After one more sanding, three layers of spray paint get applied followed by a clear coat which completes the treatment. The surface treatment successfully results in a smooth, well-finished surface. However due to the time-consuming nature of the process and added weight, the team decided to forgo using it for the final vehicle. Figures 20, 21 and 22 show the surface treatment process.

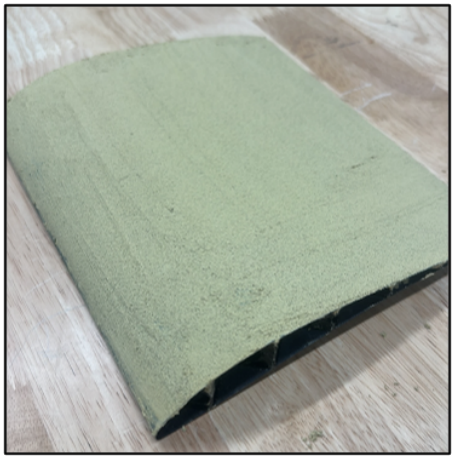

Fig. 20 Wing with Wood Filler

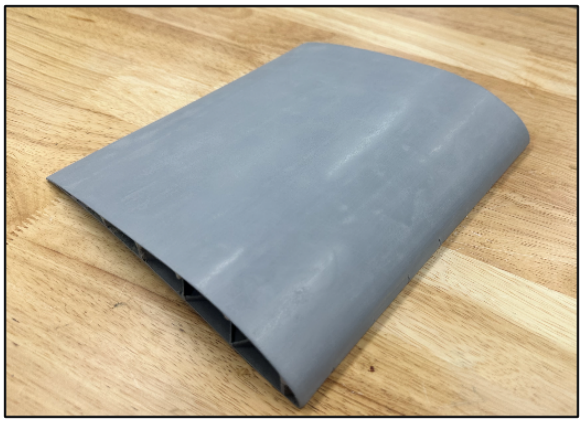

Fig. 21 Wing with Primer

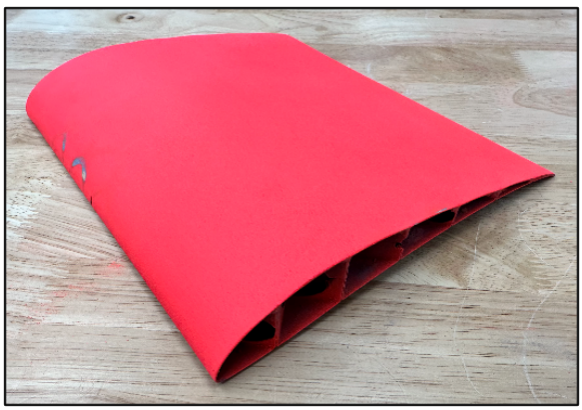

Fig. 22 Wing Painted

PETG is used for the wingtip sections and fuselage. PETG is chosen for its high strength and impact resistance, essential for parts transferring loads between the carbon fiber structural spars and booms. Threaded aluminum end caps are manufactured using

a lathe and epoxied into the ends of the carbon fiber tubing. This allows the 3D printed components to be firmly affixed to the spars and booms (Figure 23 and Figure 24). Furthermore, holes are drilled through the booms through which screws are inserted to securely lock the 3D printed components to the spars and booms as an additional fixing measure.

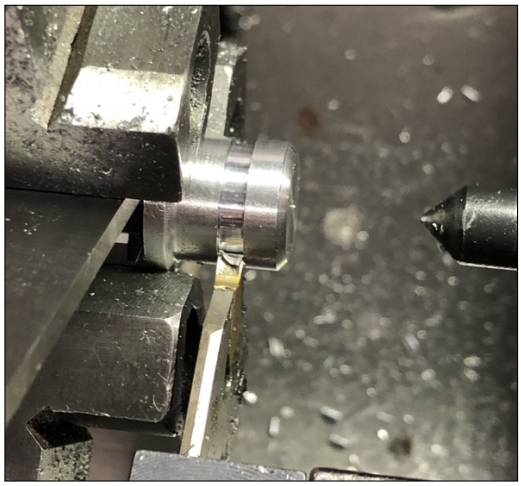

Fig. 23 Machining the Endcaps

Fig. 24 Endcaps Epoxied into Spars

Similarly, the fuselage is produced in a segmented fashion, with each section printed individually and then joined together using aluminum spars. This method mirrors the wing construction, ensuring uniformity in manufacturing processes and material properties across the vehicle. The segmented approach to the fuselage allows for a high degree of customization and adaptability in the design. It also simplifies the repair process, as damaged sections can be easily replaced without the need for extensive overhauls.

5.2 Motor Mounts. The motor mounts are manufactured from PETG since it is a critical component. The motor mounts join the motors to the booms and the landing gear. The use of redundant affixing mechanisms ensures the motors are secure on the aircraft. These include a screw that goes through the mount and the booms, a screw clamp that tightens the mount around the boom, and a screw that goes through the aluminum endcap that is epoxied into the carbon fiber.

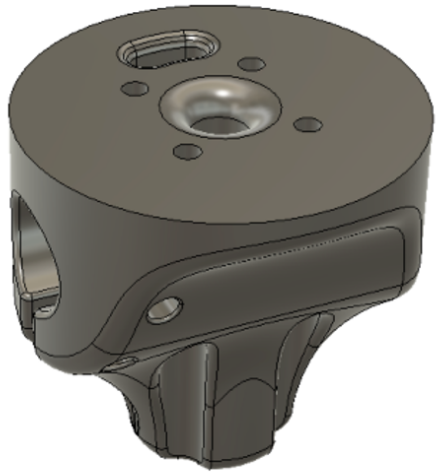

Fig. 25 Motor Mount CAD Drawing

Fig. 26 Motor Mount

5.3 Batteries. A 16000mAh 6S (22.2V) HRB LiPo (Figure 27) battery pack is used to power the propulsion system. In between the battery and propulsion system are the shunt plug, and battery monitor. The battery monitor continuously tracks the battery's remaining charge and the rate of power consumption. The battery monitor enables automatic alerts to the pilot of autopilot module when the battery capacity falls below a certain threshold. This allows for a safe intervention, enabling the pilot to initiate a controlled descent and landing. A 2200mAh LiPo battery is used to power the flight control system (Pixhawk and peripherals).

Fig. 27 16Ah LiPo HRB Battery

5.4 Electronics and Avionics. A Pixhawk 6C is used as the onboard flight controller as shown in Figure 28. The Pixhawk has an onboard IMU (inertial measurement unit) and barometer. The onboard IMU has an accelerometer, which measures acceleration in each of the three translational axes, and a gyroscope, which measures acceleration in each of the three rotational axes. The barometer is used to estimate the altitude using the surrounding air pressure.

For the manual control segment of the competition, a Radiomaster TX16S remote control is used to send commands to the vehicle, as shown in Figure 29. An FrSky Taranis Receiver X8R (Figure 30) is used to establish a connection between the remote control and the Pixhawk. An M10 GPS Module (Figure 31) from Holybro is used for position tracking. The GPS Module has a built-in compass, for orientation tracking. Two 100mW, 916mHz SiK Telemetry Radios (Figure 32) are used to establish connection between the Pixhawk and the ground station. The two telemetry radios operate on an open-source radio platform that allows for ranges of up to 300m. The telemetry radios have been specifically designed to be integrated with QGroundControl and PX4 Autopilot.

Skywalker 80A V2 Electronic Speed Controllers (ESCs) are used to control the aircraft motors (Figure 33). The ESCs' ability to handle substantial current pass-through was an important factor, ensuring the drone operated efficiently under high-current conditions. The connectors of the ESCs fit with the motor pins and the ESC has a simple calibration process. The option for digital control, although not utilized, offered flexibility to upgrade control methods without needing additional hardware

Fig. 28 Pixhawk 6C

Fig. 29 TX16S Controller

Fig. 30 FrSky X8R Receiver

Fig. 31 M10GPS

Fig. 32 SiK Telemetry Radios

Fig. 33 Skywalker 80A V2 ESC

5.5 Autonomous Flight. QGroundControl (QGC) [6] is used as our ground control station to configure flight paths, and to monitor the aircraft during flight. QGC's extensive telemetry allows for control and observation over every aspect of the mission. QGC's simulation tools enable pre-flight testing and optimization, enhancing safety and performance. QGC is also chosen due to its compatibility with a wide range of autopilot systems, and extensive autopilot tuning tools. An example of the home screen can be seen in Figure 34.

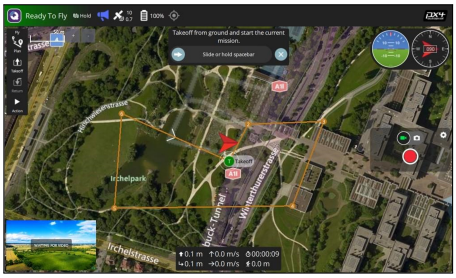

Fig. 34 QGroundControl Home Screen

5.6 Systems Layout. The aircraft's electrical system layout is shown in Figure 35. As per competition guidelines, two separate batteries are used to power the propulsion system and the autopilot system. The battery monitor is connected in between the propulsion system battery and power distribution board. Its signal wires are connected to the Pixhawk, and provide vital battery information, without directing any of the power from the propulsion battery to the Pixhawk. The Electronic Speed Controllers are powered via a Power distribution board and receive signals from the Pixhawk.

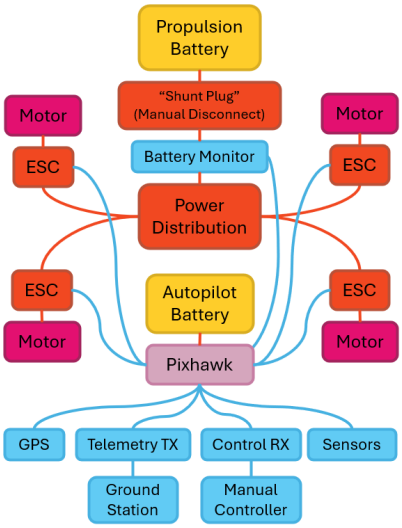

Fig. 35 Systems Layout

6 Manufactured Vehicle Images

Fig. 36 Fuselage

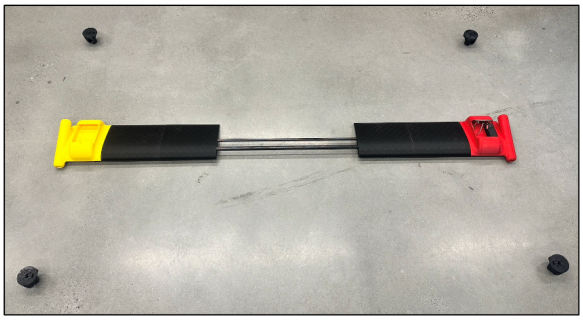

Fig. 37 Wing Assembly

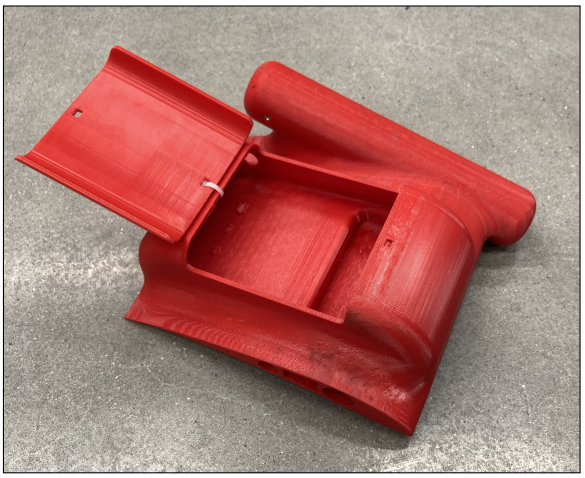

Fig. 38 Wingtip

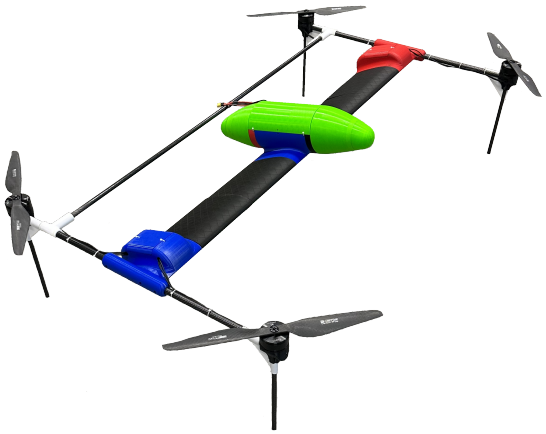

Fig. 39 Fully Assembled Vehicle

7 Testing

7.1 Drone Lab Testing Protocol. Drone Lab Testing Protocol The following testing protocol is for testing within the Drone Lab. Essential priorities of testing are safety of personnel and equipment on site. To maintain the safety required, communication is essential. All persons located in the lab will be notified before any

testing begins and asked to leave if they are not essential to the test.

7.1.1 Preflight checks.

(1) Remove all propellers.
(2) Confirm all the motors are plugged into the ESCs and that the ESCs are connected to the propulsion battery.
(3) Confirm all pre-flight checks pass in QGroundControl.

7.1.2 Motor tests.

(1) All persons except the team and authorized test supervisors must be behind the net curtain in the lab
(2) All persons in the lab must be wearing eye protection
(3) Yellow Lab test light must be on and flashing
(4) Run the independent motor spin tests - spin each motor one by one, confirm that the correct motor spins each time.
(5) Arm the transmitter - the propellers should spin at 10 percent throttle.
(6) Confirm e-stop works.
(7) Confirm the remote e-stop works:
    (a) Disarm should instantly turn off the motors.
(8) Re-arm and confirm shunt plug works:
    (a) Confirm that pulling the shunt plug cuts power to the props.
        i. Do this while in arming mode.
        ii. Pull the shunt plug cable from outside of the safety netting of the lab to ensure it will work properly during propeller tests.

7.1.3 Rotational tests.

(1) Reinstall the shunt plug and make sure the motors are disarmed.
(2) While the motors are disarmed complete the following steps. Ensure that any devices which could turn on the motors are securely isolated from anyone and will not be handled until this step is complete.
(3) Place the test stand on the ground in a central location and insert the counterweight on top of the base plate.
(4) Support the legs of the vehicle as it is placed in position over the fuselage interface.
(5) Use the yellow straps to securely fasten the vehicle to the fuselage interface.
(6) Remove the leg supports and let the vehicle tilt forward or back until it rests on two legs.
(7) Install the propellers.
(8) All persons must be located behind the safety netting.
(9) Red Lab test light must be on and flashing
(10) Turn on motors and ensure that the vehicle can obtain a stable horizontal orientation.

7.2 Static Motor Current Draw Measurement. In this test, static tests using only the motor, electronic speed controller, flight controller, battery, and handheld radio transmitter were conducted. During this test, a single motor was connected to an ESC and the battery. The radio was connected to the receiver, which was plugged into the Pixhawk flight controller. As the throttle on the radio was increased, the current draw was monitored. For this test, the motor was fixed and clamped to the table, and all team members were outside the room, for safety reasons. It was determined that all parts were functioning properly. Battery voltage and power consumption reading were accessible from the ground station. The current draw of the motor was measured as the throttle was changed to get a baseline for future thrust measurements. To charge the battery, an HTRC T240 Duo charger was used. This charger allowed us to choose a custom charging rate, and battery capacity. This was important to ensure the batteries charged safely, and without causing any damage to the batteries themselves.

7.3 Fail-safe Mechanisms Operational. While securely attached to a test bench, the operation of both fail-safe mechanisms was ensured. First, the lost-link power cut functionality of the remote controller. Second, the operation of the shunt plug, a manually operated physical disconnect between the propulsion battery and propulsion system seen in Figure 40. To test both fail-safe mechanisms, the plane's propellers were connected to power, team members moved behind the net (and all non-team members left the room), and the vehicle was armed. When armed, the aircraft's propellers spun at about 10% throttle. To test the eStop fail-safe, the remote control was turned off, while the propellers were still armed. Right after the remote shut off, the propellers came to a stop. To test the shunt plug, a similar test was done, but instead of turning off the remote, the shunt plug was pulled while the propellers were armed. This caused the power from the propulsion battery to no longer be able to deliver power to the propellers, thus instantly stopping the propellers.

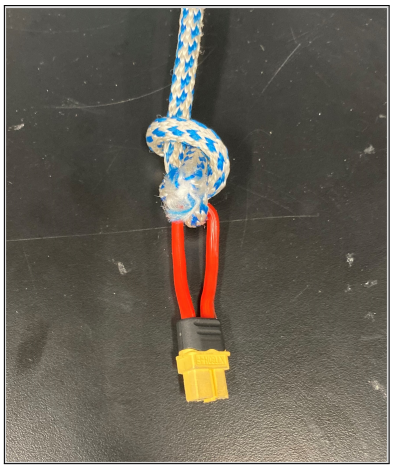

Fig. 40 Shunt Plug

7.4 Test Bench Full RDOF Control. To test control of all rotational degrees of freedom, a rotational test stand was constructed. The base of the test stand is made of plywood pieces oriented in a pyramid structure. A 3D-printed rotation point bolts the plywood braces together at the top of the pyramid. The construction can be seen in Figure 41. The fuselage of the vehicle straps to another 3D printed element which matches the contour of the fuselage bottom. The fuselage attachment is displayed in Figure 42. It slopes down to a point where an aluminum rod is mounted. The aluminum rod is epoxied into a spherical bearing which slots into the top section of the base. This allows the vehicle to rotate in all directions while limiting the maximum rotation from level flight.

7.5 Indoor Hover Stability. Once the inner control loops for the vehicle were tuned and stable testing on the gimbal was observed, the vehicle was removed from the gimbal and allowed to take off indoors. Each leg of the aircraft was tied off to a heavy stationary object to ensure safety. During the test, the vehicle was able to lift off and attain a steady hover, but the ropes attached to the legs of the drone caused it to oscillate laterally between extremes without any control input. This behavior was not replicated outside the lab environment.

7.6 Outdoor Hover Stability. The outdoor hover stability test was conducted on April 9th, 2024 in Johnson Park in Piscataway NJ, the day before our final competition. This was an extension of the same indoor hovering capabilities to a safe, open area with additional air disturbances. During this test, the team practiced constructing the entire aircraft from scratch for the first time in preparation for the competition. Initial testing was inconclusive;

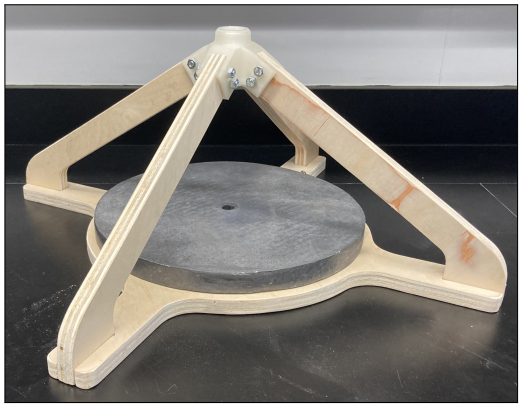

Fig. 41 Test Stand Base

Fig. 42 Fuselage Attachment

the aircraft was unable to lift off the ground. It was noticed that one side of the plane was lifting off before the other, but testing proceeded. Eventually, one side of the plane lifted off before the other and the slightest instability caused the plane to flip over onto its back. The reason for the plane flipping over was not discovered until the next day at competition.

With minimal structural damage to the plane, the plane was disassembled, and the team returned to the hotel. The aircraft's flipping over was attributed to the uneven ground at the park.

Fig. 43 Flipped Plane

8 Competition

At competition, the issue from the previous day was discovered while the team was assembling the drone. Checking the signal wiring for each of the motors, it was not consistent with the expected wiring in the motor control software. The wiring for the front and back left motors had been crossed. This caused one side of the plane to lift before the other as observed.

The team was immediately faced with a subsequent issue when the drone was weighed. Unexpectedly, it was 1.5 pounds over the 20-pound weight limit. This is likely due to the measurement approach taken in the lab. A single 6-inch diameter table scale was placed on the floor and the entire aircraft had to be balanced to weigh it. This technique clearly had enormous error involved. The immediate solution to this problem was to remove any unnecessary pieces of the plane. The team identified that it was possible to remove two cross-beams between the legs without affecting the vehicle too much. While they added some structural rigidity, they were the least essential element and the easiest to remove. This afforded just enough weight savings to pass the check.

After passing the weight check, it was time to fly the vehicle. Following all procedures, it took off and was hovering successfully when suddenly all motors cut out for a moment and it dropped to the ground before starting up again. The behavior was suspicious so we stopped flying and investigated. When the shunt plug was removed after the test, it was unusually warm. Inspecting the plug, we recognized that a portion of the wires were open to the air which had been identified several weeks prior. In the meantime the drone was working as expected however, so it wasn't evaluated as a problem. This time, the plastic insulation around the wires had melted significantly and scorched further. While in flight, a spark must have jumped between the wires, temporarily interrupting the current flow somehow. It is still uncertain why the short had the effect that it did, but it was definitely not safe for the electronics. Some gracious students from other teams provided the supplies needed to replace the part. With this part replaced, the circuitry issues were resolved.

The final unrecoverable blow to the drone was a gust of wind that excited the vehicle's torsional mode. The oscillation of the booms grew and the vehicle became unstable before falling to the ground and breaking several parts. Even if the team was able to repair the broken pieces, it was clear that the inherent torsional rigidity limitations of the vehicle would not allow it to fly.

Fig. 44 Problem Solving at Competition

9 Design Improvements

As mentioned, the plane failed due to torsional bending and it is assumed that it is an issue with the connection point between the wing spars and the propeller booms. The original connection shown in Figure 45 features a circular aluminum endcap that was machined and epoxied into the wing spars. The end of that endcap has a threaded hole so that the last 3D printed wing section can be affixed to the booms.

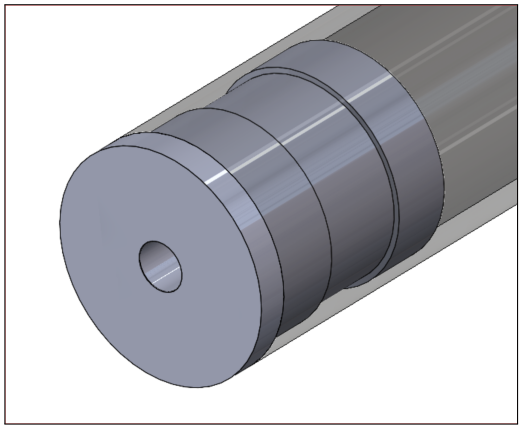

Fig. 45 Old Endcap Design

One problem with this design is that it doesn't constrain the rotation of the spars individually. Since the endcap is circular and it is fit into a circular slot, even though it is screwed against the wing section, there might be some room for it to move and cause the overall structure to be in torsion.

The solution to this problem was to make the endcap have an extruded square profile as shown in Figure 46. When inserted into a matching square profile and screwed in, it will contain the rotation and any rotation in the plane should come from torsion in each individual beam which is minimal.

Additionally, extra ridges were added to the endcap to provide more surface area for the epoxy and result in a stronger connection. A hole in the spar was also made so even if the epoxy inside dislodges, the epoxy that fills the hole will prevent rotation or separation of the endcap from the spar.

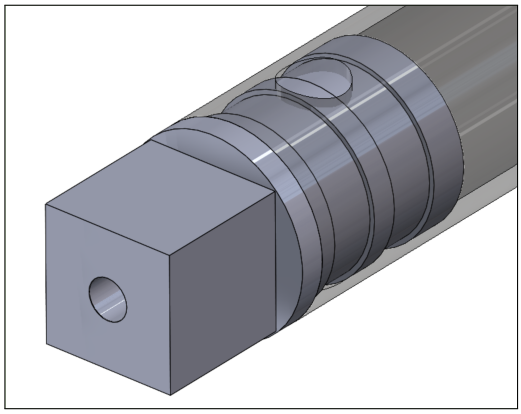

Fig. 46 New Endcap Design

10 Failure Analysis

After building the vehicle, it was clearly recognizable that the structure of the vehicle was not rigid. When lifting the vehicle from either end of the wing using the two propeller booms, the relative rotation of either side was noticeable. Even before testing the vehicle on the gimbal, fixes were attempted to remedy the issue using additional bracing and spars that connected the two booms. A one-half inch carbon tube was used with a 3D printed snap mechanism to span the width of the vehicle behind the fuselage. The snap mechanism has a blind hole on one end to fit the lateral tube and ends in a T-junction with a C-shaped cross section that snaps and grips on the perpendicular boom. The lateral tube has a snap on both sides to attach to both booms and is fixed in the middle with a zip tie to the rear of the fuselage. Additional quarter-inch carbon tubes were used to span the lateral gap between the front and back sets of legs. A 3D printed L-shaped foot with a blind hole down through the center of each segment allows the lateral tubes to be affixed perpendicular to the legs.

With these additions completed, initial tests began with the vehicle installed on the gimbal. During the tests, the propellers lifted all four legs of the vehicle off the ground and allowed control of the pitch, roll, and yaw within a certain margin. Whenever a leg of the vehicle would hit the ground, oscillations of the booms relative to one another were clearly visible. In response, impact hammer testing was performed to determine the natural frequency of the torsional mode. Figure 47 displays the measured frequencies of 3.8 and 9.2 Hz.

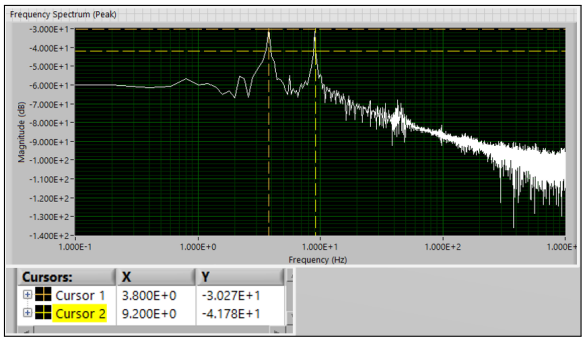

Fig. 47 Torsional Natural Frequency Measurement

In order to avoid instability, the feedback controller of the vehicle must not excite the torsional natural frequency. If the controller is allowed to output at this frequency, it will excite the vibration and cause runaway behaviour as the system will become nonlinear and not respond as the controller expects it to. One way to accomplish this to tune the controller such that the closed-loop bandwidth of the system is below this natural frequency. This was accomplished in the gimbal testing when tuning the PID gains. For each rotational degree of freedom (roll, pitch, yaw), the gains were tuned manually until desired response was achieved via visual observation. The process began with very low proportional, integral, and derivative gains and which were each increased slowly. At each increment, a step disturbance from equilibrium was given to the system using the manual controller the speed at which the vehicle came back to the origin was observed.

In both pitch and roll, the final chosen gains did not excite the torsional mode. Analysing the forces acting on the vehicle, a pitch input increases the thrust provided by the rear motors and decrease the thrust of the front motors. An equal input on both sides of the drone does not cause an opposing torsional force. A roll input increases thrust on one side of the drone while decreasing thrust equally on the other side. The net torque at the center of each boom remains zero and there will only be bending in the central spar.

In order to provide independence between pitch, roll, and yaw in a quadcopter drone, the motors alternate between spinning clockwise (CW) and counterclockwise (CCW). If the front right motor spins CW, the front left and rear right spin CCW and the rear left spins CW. With a yaw input intended to rotate the drone CW, the CW motors decrease thrust and the CCW motors increase thrust. The reaction forces on the drone from the motors cause a net CW torque about the center of mass, rotating the vehicle while it remains balanced in the pitch and roll direction. When this occurs, there is a net torque on the right side in one direction and a torque on the left side in the opposite direction. This inherently excites the torsional mode of vibration, which was observed when tuning the yaw control. However, the desired speed of response was achieved without causing the vehicle to reach instability. When the system was given an impulsive yaw signal from the controller, the

vibration caused by it was visible, but the system remained within its linear region and the vibration was damped enough to return to equilibrium.

With the control loops tuned, the next step was to bring the drone to permitted airspace and do hover testing. The first real opportunity to do this was at competition, where several factors resulted in the drone having less stiffness than we designed for. First, in order to meet the takeoff weight limit the spars spanning the feet of the vehicle were removed. It is questionable whether these parts provided much stiffness, but removing them definitely reduced it. More importantly, the metal end caps in the rear wing spar broke loose, reducing the stiffness further. The end caps breaking loose meant that the rear spar was able to rotate freely in the wingtip section, effectively eliminating the torsional stiffness provided by that element.

As described previously, when the drone finally flew, a wind gust disturbance excited the torsional mode and the oscillation became unstable resulting in the drone crashing. Reviewing the footage, the oscillation frequency is identified as 2.15 Hz, which is significantly lower than the frequency determined by vibration testing. Figure 48 depicts the motion of the rear motors relative to the center of mass of the drone, with amplitude as an arbitrary unit of measure in this case. The right boom data is flipped across the amplitude axis to improve visual clarity. An exponential sinusoid curve is fit numerically to the data to identify the frequency of oscillation.

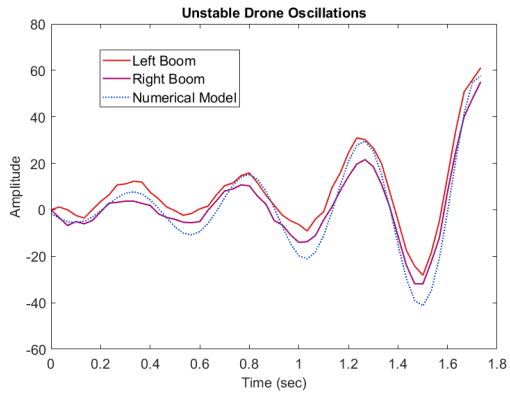

Fig. 48 Oscillations Leading to Crash

In order to determine an appropriate solution for the issue, it is relevant to model the expected natural frequency of this system. The simplified model chosen for the following analysis is a set of three torsional springs acting in parallel to support the propeller boom. It is assumed that the boom rotates about the center of the larger wing spar. The larger wing spar provides some torsional stiffness while the smaller spar provides both torsional and bending stiffness.

The measured parameters of the system are as follows. The mass of the motors, mounts, and legs is treated as a point mass of $0.521kg$. The mass of the boom is $0.131kg$. The length of the boom is $0.914m$. The length of both wing spars is $1.50m$". The radius of the larger wing spar is $9.5mm$, while the smaller is $6.4mm$. The wall thickness of both rods is $1.6mm$. The carbon fiber rods are roll-wrapped. The estimated Young's Modulus is $90GPa$ and Shear Modulus is $4.6GPa$ [7].

The polar moments of inertia of the rods are calculated using the following formula:

$$J = \frac{\pi}{2}\left(r_o^4 - r_i^4\right)$$

The moment of inertia of the smaller rod about the neutral axis is:

$$I_{tube} = \frac{\pi}{4}\left(r_o^4 - r_i^4\right)$$

The moment of inertia of the boom and motor system about the rotation point is:

$$I_{boom} = 2m_{motor}\,(0.5l_{boom})^2 + \frac{1}{12}m_{boom}l_{boom}^2$$

The torsional stiffness of each spar is:

$$k_T = \frac{G_{cf}J_{tube}}{0.5l_{spar}}$$

The bending stiffness in torsion of the rear spar is:

$$k_B = \frac{3E_{cf}I_{tube}}{d_{spars}(0.5l_{spar})^3}$$

Where d_{spars} is the distance between the two spars.

Two cases are considered for calculating the natural frequency of torsional vibration. The first option is to consider all stiffness components acting in parallel. The second is to neglect the smaller rod, which resembles the behavior of the system with the broken end caps on the smaller rod. In the first case, the total stiffness of the system is given by $k = k_{T,L} + k_{T,S} + k_{B,S}$, where L and S denote the large and small spars. In the second case, $k = k_{T,L}$.

The governing equation for this oscillatory behaviour is:

$$I_{boom}\ddot{\phi} + k\phi = T$$

Where T is the torque from the motors acting on the system and I is I_{boom} The natural frequency of the system (in hertz) is:

$$f_n = \frac{1}{2\pi}\sqrt{\frac{k}{I}}$$

The natural frequencies in each case are $f_{n,1} = 3.26Hz$ and $f_{n,2} = 2.15Hz$.

Comparing the results of this model with the measured real-world frequencies, in case one the natural frequency is somewhat lower than the 3.8Hz frequency measured in the lab. This is probably due to the fact that the bending stiffness of the front spar was excluded from the stiffness calculation under the assumption that the boom rotates around it. In reality the boom rotates at a point between the two spars.

In the second case, the natural frequency aligns perfectly with the measured oscillation from the competition flight. While the drop in stiffness would cause the natural frequency to decrease, the fact that the value matches perfectly is only coincidental. The assumptions made in the model are not entirely accurate to reality. The lengths chosen do not correspond to the exact boundary conditions. The carbon fiber properties are from a third party source. The bending stiffness of both spars contributes even if the end cap breaks. Beyond the model, it is important to note that the oscillation of the drone is the response of the closed-loop system using a feedback controller which is not equivalent to the natural frequency.

An important conclusion to draw from the model is that even with a perfectly rigid connection at the wingtips between the spars and the boom, the natural frequency of the system is still quite low. The drone must remain stable while responding quickly to disturbances such as wind gusts. Ideally, the bandwidth of the controller should be in the range of 3-10Hz if not higher. Any frequency of oscillation should be greater than the bandwidth. This means that even with the design improvements, it is unlikely that the drone can achieve stable flight. A larger redesign is necessary to make this concept come to life.

11 Future Senior Projects

We believe the VFS DBVF Competition is an excellent opportunity for future Mechanical Engineering senior project teams to synthesise the knowledge learned throughout the curriculum. The competition demands mastery and ingenuity across multiple areas of the mechanical engineering curriculum including design, structural mechanics, aerodynamics, and controls.

If a future senior project team wishes to partake in this competition, our advice would be to start testing as early as possible. It is important to create a design you think will work, but no matter how much time is spent calculating and theorizing there will always be unanticipated issues when all the parts are put together and you try to fly.

A team that takes on this challenge will have access to all the materials used from both our year and the previous. We are happy to share all our research and calculations. During the competition, the team and Professor Wootton determined a toolbox list of needed equipment so as to be prepared for unexpected situations. We believe that the design concept used in our attempt is potentially a very energy and resource-efficient solution to the problem set forth by the competition. We hope that a future team takes it further by redesigning and rebuilding to address the structural rigidity issues with the vehicle.

References

[1] Doddi, A., 2016, "Vertical Take-off and Landing (VTOL)," University of Colorado Boulder, Retrieved from https://www.colorado.edu/faculty/kantha/sites/default/files/attached-files/158128-154174_-_abhiram_doddi_-_dec_13_2016_228_pm_-_doddi_report.pdf.

[2] Bellamy, W., 2021, "10 eVTOL Development Programs to Watch in 2021," Avionics International, Retrieved from https://interactive.aviationtoday.com/avionicsmagazine/february-march-2021/10-evtol-development-programs-to-watch-in-2021/.

[3] Harris, F. D., 2015, "Introduction to Autogyros, Helicopters, and Other V/STOL Aircraft," NASA Technical Reports Server (NTRS), Retrieved from https://ntrs.nasa.gov/api/citations/20190000456/downloads/20190000456.pdf.

[4] Vertical Flight Society, 2023, "2023-2024 Design-Build-Vertical Flight Competition: Request for Proposal," Vertical Flight Society, Request for Proposal Rev 2.2.

[5] Archives, N., 2013, "Part 15-Radio Frequency Devices," Code of Federal Regulations, Retrieved September 30, 2013, from https://www.ecfr.gov/current/title-47/chapter-I/subchapter-A/part-15.

[6] QGroundControl Development Team, 2023, "QGroundControl," Open Source Software, Version 4.2, available at http://qgroundcontrol.com.

[7] EasyComposites, 2024, "34.8mm (32mm) Roll Wrapped Carbon Fibre Tube," Retrieved from https://www.easycomposites.co.uk/34-8mm-roll-wrapped-carbon-fibre-tube.

[8] FrSky, n.d., "X8R," FrSky, Retrieved from https://www.frsky-rc.com/x8r/.

[9] HobbyZone, 2022, "HobbyZone RC Airplane Carbon Cub S 2," Amazon.com, Retrieved December 9, 2022, from https://www.amazon.com/HobbyZone-Airplane-Battery-Included-HBZ320001/dp/B0BPMK6QDW/ref=sr_1_2.

[10] Holybro, n.d., "Nano M8 5883 GPS Module," Holybro, Retrieved from https://holybro.com/products/nano-m8-5883-gps-module.

[11] Holybro, n.d., "Pixhawk 6C," Holybro, Retrieved from https://holybro.com/products/pixhawk-6c.

[12] Holybro, n.d., "SiK Telemetry Radio V3," Holybro, Retrieved from https://holybro.com/products/sik-telemetry-radio-v3.

[13] Autopilot, P., 2023, "Holybro Pixhawk 6C," PX4 User Guide (main), Retrieved August 3, 2023, from https://docs.px4.io/main/en/flight_controller/pixhawk6c.html.

[14] RadioMaster, "TX16S Mark II Radio Controller (Mode 2)," RadioMaster, Retrieved from https://www.radiomasterrc.com/products/tx16s-mark-ii-radio-controller.

[15] T-Motor, "P20*6 Prop-2PCS/PAIR," T-Motor, Retrieved from https://store.tmotor.com/goods-385-P20%2A6+Prop-2PCSPAIR.html.

[16] T-Motor, "P60 Pin P Type Agricultural UAV Motor KV340," T-Motor, Retrieved from https://store.tmotor.com/product/P60-pin-kv340-p-type.html.

[17] FAA, "Small Unmanned Aircraft Systems (UAS) Regulations (Part 107)," FAA, Retrieved from https://www.faa.gov/newsroom/small-unmanned-aircraft-systems-uas-regulations-part-107.

List of Figures

List of Tables